




 Cite this: *RSC Adv.*, 2022, **12**, 31985

A highly active Z-scheme SnS/Zn₂SnO₄ photocatalyst fabricated for methylene blue degradation†

 Yingjing Wang, Fen Xu, * Lixian Sun, * Yaying Li, Lumin Liao, Yanxun Guan, Jianhao Lao, Yukai Yang, Tianhao Zhou, Yu Wang, Bin Li, Kexiang Zhang and Yongjin Zou

Herein, a highly active Z-scheme SnS/Zn₂SnO₄ photocatalyst is fabricated by a one-step hydrothermal route. The structure, composition, photoelectric and photocatalytic properties of the as-prepared photocatalysts are systematically researched. The results demonstrate that SZS-6 displays a good photocatalytic performance with an efficiency of 94.5% to degrade methylene blue (MB) under visible light irradiation ($\lambda > 420$ nm). And its degradation rate constant is up to 0.0331 min⁻¹, which is 3.9 and 4.4 times faster than SnS and Zn₂SnO₄, respectively. The formation of a Z-scheme heterojunction facilitates the separation and transfer of charges, which improves the degradation of MB. The Z-scheme charge transfer pathway of the SnS/Zn₂SnO₄ photocatalyst is verified by the shifted peaks of the X-ray photoelectron spectroscopy (XPS) spectrum, the relative position of the bandgap, work function as well as free radical trapping experiments. The photocatalytic mechanism for the degradation of MB by SnS/Zn₂SnO₄ is proposed.

Received 2nd September 2022

Accepted 19th October 2022

DOI: 10.1039/d2ra05519h

rsc.li/rsc-advances

1. Introduction

Various semiconductor materials, such as metal oxides (TiO₂),^{1,2} bimetallic oxides (Zn₂SnO₄),³ sulfides (CdS),⁴ complex oxides (Bi₂WO₆)⁵ and non-metallic material (g-C₃N₄),^{6,7} have been studied as photocatalysts in the field of the degradation of organic pollutants,⁸ hydrogen production⁹ and nitrogen reduction.¹⁰ Organic pollutants, such as those in textile wastewater, have impacted water resources severely. It is imperative to purify the water of organic pollutants by photocatalytic degradation technology.^{11–13} Among them, Zn₂SnO₄ has high electrical conductivity, abundant active sites, and excellent optical properties, making it stand out among many semiconductor materials.

Zn₂SnO₄ has promising applications in functional optoelectronic devices, gas-sensitive materials, photocatalytic oxidation of organic pollutants, and solar cells.^{14–17} However, the Zn₂SnO₄ needs to be excited under UV light because of its wide bandgap. And then, Yan *et al.* successfully prepared the p-BiOI/n-Zn₂SnO₄ heterojunction.¹⁸ They found that the optical absorption edges of p-BiOI/n-Zn₂SnO₄ shifted from 345 to

650 nm, and nearly 100% of methylene blue (MB) was degraded under visible light. Nonetheless, the complicated charge transfer pathway and high carrier recombination rate of the p–n heterojunction still limited its application in photocatalysis.

Inspired by natural photosynthesis, the construction of Z-scheme heterojunctions has attracted considerable attention in photocatalysis. Because they can efficiently transfer and separate photogenerated carriers while maintaining outstanding redox ability.^{19–21} The conventional Z-scheme photocatalysts are generally constructed using external carrier media.^{22–24} Ye *et al.* synthesized a Z-scheme Ag/AgBr/BiOBr photocatalyst with Ag as the electron medium. They found that the Ag/AgBr/BiOBr photocatalyst exhibited enhanced photocatalytic performance for RhB degradation.²⁴ Nevertheless, these mediators may hinder the light absorption of the composites or lead to backward reactions.^{25–27} Therefore, developing a direct Z-scheme photocatalytic system is desired.

As one known, SnS shows a light absorption factor over a broad-spectrum range and has the advantages of non-toxicity and high chemical stability. However, pure SnS is easy to deactivate under visible light irradiation, with poor electron transfer ability and fast charge recombination rate. Therefore, it is commonly introduced into some photocatalyst systems (*e.g.*, ZnO,²⁸ Bi₂WO₆,²⁹ TiO₂³⁰) to expand the light absorption range and promote the separation of photogenerated carriers. Jayswal *et al.* inserted SnS nanoparticles on the ZnO nanorod surface to achieve the ZnO/SnS.²⁸ It indicated that the absorption of sunlight by ZnO/SnS was enhanced, and the photocatalytic

Guangxi Key Laboratory of Information Materials, Guangxi Collaborative Innovation Center for Structure and Properties for New Energy and Materials, School of Material Science and Engineering, Guilin University of Electronic Technology, Guilin 541004, P. R. China. E-mail: xufen@guet.edu.cn; sunlx@guet.edu.cn

† Electronic supplementary information (ESI) available. See DOI: <https://doi.org/10.1039/d2ra05519h>



degradation efficiency increased from 0.0035 min^{-1} (ZnO) to 0.0212 min^{-1} (ZnO/SnS). Therefore, SnS could act as a photosensitizer to improve the solar absorption efficiency of semiconductors. SnS/Zn₂SnO₄ is currently used in sensor-related applications and has not been studied in photocatalysis.^{31,32}

Herein, a direct Z-scheme SnS/Zn₂SnO₄ photocatalyst was successfully synthesized by a one-step hydrothermal route. The phase structure, photogenerated electron-hole pairs transfer and separation of SnS/Zn₂SnO₄ were investigated. The results demonstrated that the degradation rate constant of MB by SZS-6 reaches 0.0331 min^{-1} under visible light, corresponding to 94.5% degradation in 60 min. Based on the experimental results and bandgap structure analysis, the photocatalytic mechanism of SnS/Zn₂SnO₄ was researched.

2. Experimental

2.1. Materials

All chemicals were used in analytical grade in this experiment. The chemicals used were L-tryptophan (C₁₁H₁₂N₂O₂), SnCl₄·5H₂O, Zn(Ac)₂·2H₂O, NaOH, HCl, methylene blue (MB), Rhodamine B (Rhb), Methyl Orange (MO), SnS, benzoquinone (BQ), isopropanol (IPA, 99.0%), ethylene diamine tetraacetic acid disodium (EDTA-2Na) and ethanol absolute, which were purchased commercially. Deionized (DI) water was used to prepare all solutions for the experiment.

2.2. Preparation of SnS/Zn₂SnO₄ composite

L-Tryptophan (0.3 g) was dissolved in deionized water at 60 °C. Then SnCl₄·5H₂O (0.2214 g) and Zn(Ac)₂·2H₂O (0.263 g) were added to the above solution. A NaOH solution (0.058 g mL⁻¹) was dropwise added to adjust the pH of the mixed solution to 10 during stirring. And the mixed solution was continued to stir for 30 min. Then, a certain amount of well-dispersed SnS was added to the solution and went on stirring for 30 minutes to obtain a precursor solution. The precursor solution was sealed in a 100 mL Teflon reactor. The hydrothermal reactor was carried out at 200 °C for 24 h. The precipitate obtained was washed three times with DI and ethanol absolute, then dried at 60 °C for 12 h. The final products were SnS/Zn₂SnO₄ composites, named SZS-*x* (*x* = 3, 6, 9 and 12%); in which *x* is the weight ratio of the SnS over Zn₂SnO₄. To facilitate comparison, the pure Zn₂SnO₄ was also prepared by the similar procedure mentioned above in the absence of SnS.

2.3. Characterization

The crystalline structures of samples were performed by a powder X-ray diffraction (XRD; Bruker DAVINCI D8 ADVANCE). The surface morphology of the catalysts was revealed by a scanning electron microscope (SEM; Quanta 200, FEI, American). The microstructures of the samples were characterized by transmission electron microscope (TEM; Talos F200X, FEI Company, USA) and high-resolution TEM (HRTEM). The corresponding elemental mapping of the sample was obtained on the TEM with an energy-dispersive X-ray (EDX) analyser. The chemical state of the analysis of the elements was

performed by an X-ray photoelectron spectroscopy (XPS; ESCALAB 250Xi, Thermo Fisher). The UV-vis absorption spectra were investigated by using ultraviolet-visible diffuse reflectance (DRS, Metash UV-8000). The recombination characteristics of photo-generated carriers of samples were collected by steady photoluminescence (PL) spectra on a spectrophotometer (Edinburgh FS5) under 365 nm excitation. The nitrogen adsorption-desorption isotherms of the samples were tested using a gas adsorption analyzer (Autosorb iQ2, Quantachrome sorptometer, Osaka, Japan). The specific surface areas and pore size distribution of the samples were obtained by the Brunauer-Emmett-Teller (BET) method and the Barrett-Joyner-Halenda (BJH) method, respectively.

2.4. Photocatalytic activities testing

Herein, methylene blue (MB) was used as the target contaminant to evaluate the photocatalytic degradation potential of the Zn₂SnO₄, SnS and SZS-*x*. The evaluation of photocatalyst degradation performance requires a representative dye contaminant such as MB and a 300 W Xenon lamp (JP-GHX-Xe-300, Wuxi Jiuping, China, 3.82 W cm⁻²) fitted with a light filter ($\lambda > 420 \text{ nm}$) as a visible light source. Photocatalyst degradation was performed using a sandwich beaker and recirculating water condensation system (DFY-50/30, Gongyi Yuhua, China) as a photocatalytic reactor at 25 °C and a pH of 6.8 unless otherwise specified. Photocatalyst (0.05 g) was dispersed in MB solution (50 mL, 10 mg L⁻¹), and then this mixture solution was stirred in the dark and lasted 30 minutes to achieve adsorption-desorption equilibrium. The catalytic degradation reaction lasted for 60 minutes. Every 10 minutes 3 mL of the suspension was sucked up and centrifuged, and then the supernatant was taken for evaluating the content of MB at 664 nm by a UV-vis spectrophotometer. To explore the main active species of photocatalysis, EDTA-2Na, BQ and IPA were added into the reaction system of MB degradation to interfere with the MB degradation respectively. The procedures and analytical methods were the same for MB degradation except for sacrificial agents that were added before the photocatalytic reaction. The concentrations of EDTA-2Na, BQ and IPA were 0.5 mmol L⁻¹, respectively.

2.5. Photoelectrochemical measurement

The transient photocurrent response, electrochemical impedance spectra (EIS), Mott-Schottky study and cyclic voltammetry were carried out on a CHI660E electrochemical work-station (Chenhua, Shanghai, China), using 0.2 M Na₂SO₄ as the electrolyte and a standard three-electrode system, in which the catalysts were used as the working electrode, Pt slice as the counter electrode, and Ag/AgCl electrode as the reference electrode. To prepare the working electrode, 3 mg photocatalyst was dispersed in 200 μL absolute ethyl alcohol and 5 μL Nafion (5 wt%) solution under ultrasonic for 10 min. Then, the mixed solution was dropwise added to the surface of ITO and dried at 60 °C. A 300 W xenon lamp was used as a light source for the transient photocurrent response test.

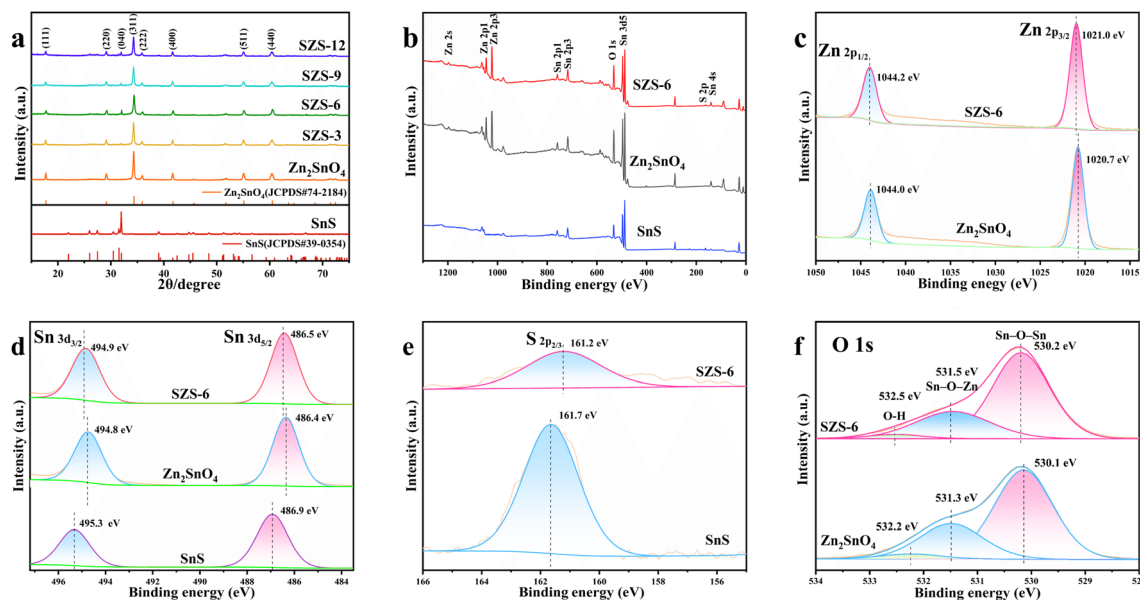


Fig. 1 (a) XRD spectra, (b) XPS survey, (c) Zn 2p, (d) Sn 3d, (e) S2p and (f) O 1s spectra of samples.

3. Results and discussion

3.1. Structure and morphology

3.1.1. X-ray diffraction and XPS analysis. Fig. 1a summarizes the XRD curves of Zn_2SnO_4 , SnS and SZS-*x*. From Fig. 1a, it is observed that each diffraction peak of Zn_2SnO_4 is in agreement with the cubic phase of Zn_2SnO_4 (JCPDS # 74-2184).¹⁸ The diffraction peaks of SnS are consistent with the orthogonal phase of SnS (JCPDS # 39-0354).²⁸ Meanwhile, the characteristic peaks of Zn_2SnO_4 and SnS appear in the XRD curve of the SZS-*x*. Moreover, no miscellaneous peaks are observed in the SZS-*x*, indicating that no other phases are formed.

The average particle sizes of Zn_2SnO_4 and SZS-*x* are computed utilizing the Scherrer formula:^{33,34}

$$D = K\lambda/\beta \cos \theta \quad (1)$$

where D is the grain size, β is the FWHM of the (311) peaks, K is the Scherrer constant ($K = 0.89$), λ is the X-ray wavelength ($\lambda = 0.154$ nm) and θ is the diffraction angle. The average particle sizes of the samples are summarized in Table 1. The particle size shows a different degree of decrease after compounding SnS and Zn_2SnO_4 . It indicates that the transfer and rearrangement of Zn, Sn, and O ions between the particles are hindered and the growth of Zn_2SnO_4 nanoparticles is inhibited, resulting in a decrease in the particle size of SZS-*x*.³³ Meanwhile, it also can be found that recombining Zn_2SnO_4 with SnS does not cause significant changes in the Zn_2SnO_4 lattice parameters.

The X-ray photoelectron spectroscopy (XPS) of Zn_2SnO_4 , SnS and SZS-6 were obtained to study the chemical state of the elements (Fig. 1b–f). As shown in Fig. 1b, four elements (Zn, Sn, S and O) are detected in the XPS spectra of SZS-6. The binding energies (1044.0 and 1020.7 eV) of Zn 2p for SZS-6 are the same as that of Zn_2SnO_4 , corresponding to Zn 2p_{1/2} and Zn 2p_{3/2},

respectively. It demonstrates that the Zn in SZS-6 is Zn^{2+} (Fig. 1c).³⁵ Comparing the Sn 3d and S 2p of peaks for the three samples (Fig. 1d and e), it can be found that there are Zn_2SnO_4 and SnS in the SZS-6.^{28,36} The O 1s spectra of Zn_2SnO_4 can be divided into three peaks. The binding energy at 530.1 eV and 531.3 eV belongs to the oxygen atom coordinated with a metal atom (Sn–O–Sn) and (Sn–O–Zn), respectively.³⁷ The peak at 531.3 eV is attributed to oxygen in absorbed water, and the binding energy at 532.2 eV is attributed to the oxygen atoms on defect atoms.³⁷ It is noteworthy that the peaks of Sn 3d and O 1s in SZS-6 are shifted to the higher binding energy compared to the pristine Zn_2SnO_4 (Fig. 1c and f), while the peaks of S 2p in SZS-6 shifted to the lower binding energy compared to pristine SnS, which illustrates the electrons flow from Zn_2SnO_4 to SnS.³⁸ However, the conventional electron should flow from SnS to Zn_2SnO_4 , the reason for this phenomenon is that SnS (−0.79 eV) has a more negative conduction band than Zn_2SnO_4 (−0.27 eV).^{35,39}

According to the literature, this reverse flow of electrons from Zn_2SnO_4 to SnS only occurs in the presence of Z-scheme heterojunctions.³⁸ The XPS results further support the coexistence of Zn_2SnO_4 and SnS, and the existence of Z-scheme heterojunctions between Zn_2SnO_4 and SnS can be inferred.

Table 1 Lattice parameters of Zn_2SnO_4 and SZS-*x* samples

Sample	d^a (Å)	a^a (Å)	D (Å)
Zn_2SnO_4	2.613	8.667	52.549
SZS-3	2.612	8.663	52.692
SZS-6	2.607	8.646	46.838
SZS-9	2.613	8.665	48.479
SZS-12	2.611	8.659	53.511

^a d is crystal spacing, and a is lattice constant.

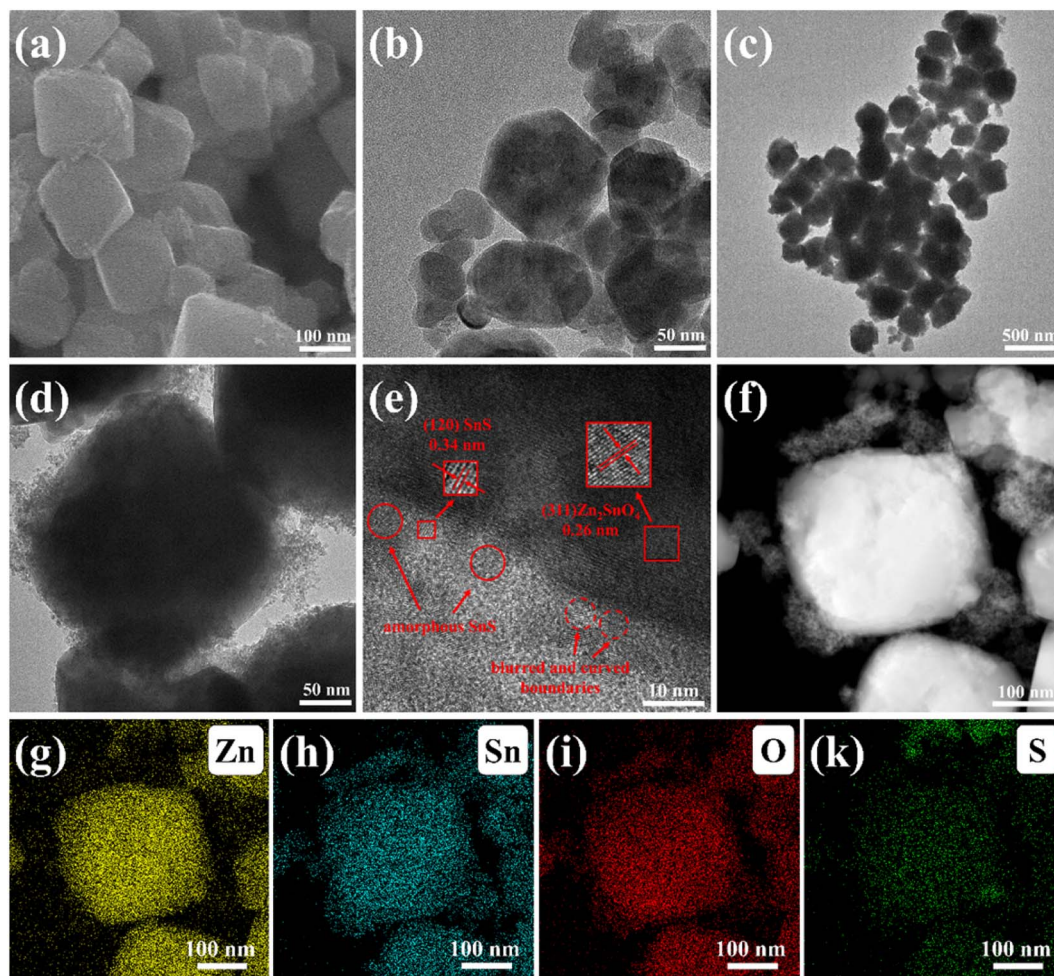


Fig. 2 (a) SEM images of Zn_2SnO_4 , TEM images of (b) Zn_2SnO_4 and (c–e) SZS-6, (f–k) HRTEM image of SZS-6 and the corresponding mapping images.

3.1.2. SEM and TEM analysis. SEM and TEM have been characterized to study the morphology of the samples. The SEM results display that the SZS-*x* still maintains the morphology of Zn_2SnO_4 , indicating doping SnS does not affect the morphology of SZS-*x* (Fig. S1†). As shown in the SEM and TEM photograph

(Fig. 2a and b), the pure Zn_2SnO_4 exhibits a cubic morphology with a mean diameter of 100–150 nm. After SnS is introduced, the morphology of SZS-*x* obtained SZS-6 particles have a diameter of about 150–200 nm and SnS particles load on the surface of Zn_2SnO_4 (Fig. 2c and d). Meanwhile, the elemental mapping

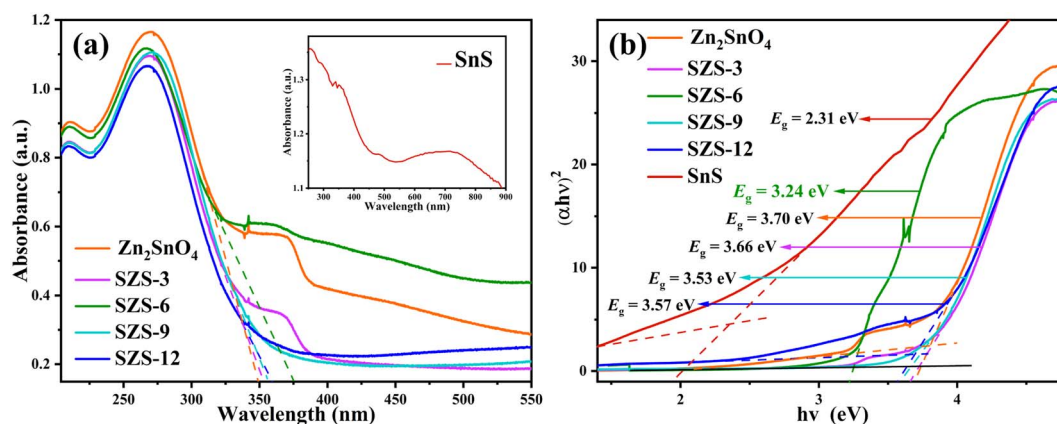


Fig. 3 UV-vis DRS spectra of the samples (a) reflectance spectra and (b) Kubelka–Munk model.

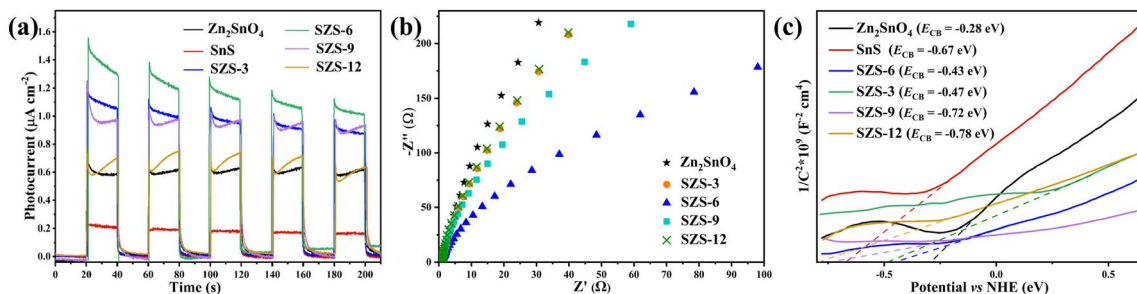


Fig. 4 (a) Transient photocurrents, (b) EIS curves, and (c) Mott–Schottky plots of samples.

images of the SZS-6 are shown in Fig. 2f–k. It can be found that S, O, Zn and Sn elements are uniform distribution. The HRTEM images of SZS-6 with d (0.26 nm) stripes match well with the (311) crystal planes of Zn_2SnO_4 (Fig. 2e), and the d (0.34 nm) stripes match the (120) crystal planes of SnS, indicating the successful fabrication of SnS/ Zn_2SnO_4 heterojunction.^{40,41} Notably, due to the weak crystallinity of SnS, some amorphous SnS marked with red circles can be seen. In addition, the lattice of SnS/ Zn_2SnO_4 appears fuzzy and curved seen in the red dashed rings in Fig. 2e, which may be due to the presence of Sn^{2+} defects, oxygen vacancy or complexes of oxygen vacancy and defect in the heterogeneous junction. It can be speculated that the structure has higher photocatalytic activity, a wider range of light-trapping ability and more active sites.

3.2. The optical properties

3.2.1. UV-vis DRS analysis. UV-vis diffuse reflectance spectroscopy (DRS) was utilized to study the optical absorption properties of the samples (Fig. 3). As shown in Fig. 3a, pure Zn_2SnO_4 can only absorb sunlight ranging from 270 to 390 nm, while SnS can absorb visible light to UV light. Furthermore, the absorption edge of SZS-6 is red-shifted compared to Zn_2SnO_4 , which indicates that SZS-6 can absorb more UV light. The bandgap energy of samples can be obtained by the following equation:⁴²

$$(\alpha h\nu)^{1/n} = k(h\nu - E_g) \quad (2)$$

where α , k , $h\nu$ and E_g are absorption coefficients, the constant, photonic energy and absorption bandgap energy, respectively. The value of n is 1/2 because Zn_2SnO_4 and SnS are all direct bandgap semiconductors.

As shown in Fig. 3b, the bandgap of Zn_2SnO_4 and SnS are 3.70 and 2.31 eV, respectively. The bandgaps of SZS- x ($x = 3, 6, 9$ and 12%) are about 3.24–3.66 eV, which are narrower than that of pristine Zn_2SnO_4 . The decrease in bandgap owes to the lattice dislocation at the interface of Zn_2SnO_4 and SnS, which forms a new intermediate energy level and reduces the bandgap energy.⁴³ It also proves that the heterojunction is formed between Zn_2SnO_4 and SnS.

3.2.2. Photoelectrochemical experiments. To investigate the production and separation of photogenerated carriers, the transient photocurrents of Zn_2SnO_4 , SnS and SZS- x were measured. As shown in Fig. 4a, the current density of pure

Zn_2SnO_4 is $0.6 \mu\text{A cm}^{-2}$, higher than that of pure SnS ($0.2 \mu\text{A cm}^{-2}$). The photocurrent intensity increases and then decreases as the ratio increases. The SZS-6 exhibits the strongest photocurrent intensity ($1.2 \mu\text{A cm}^{-2}$), which is six times higher than that of pure SnS. Usually, EIS is measured to illustrate the transport process of photogenerated carriers. It is known that the smaller arc radius of the EIS demonstrates faster charge transfer efficiency.⁴⁴ It can be found in Fig. 4b that the arc radius of Zn_2SnO_4 is the largest, while SZS-6 has the smallest arc radius and the fastest charge transfer rate. To get a deep insight into the construction of band edge position for Zn_2SnO_4 , SnS and SZS- x , the Mott–Schottky experiment was studied (Fig. 4c). The results indicate that the Zn_2SnO_4 , SnS and SZS- x are all n-type semiconductors.⁴⁵ The flat-band potential of Zn_2SnO_4 , SnS and SZS-6 are calculated to be -0.28 , -0.67 and -0.43 eV vs. NHE, respectively (Fig. 4c). According to the Mott–Schottky equation, the carrier density of the sample is proportional to the slope of the Mott–Schottky diagram.^{46,47} The SZS- x samples exhibit smaller slopes than pristine Zn_2SnO_4 , namely higher charge density. Besides, the SZS-6 shows a minimum slope, implying that the SZS-6 achieves the best charge separation efficiency.⁴⁷ Based on Fig. 3b and 4c, the bandgap energy (E_g) of Zn_2SnO_4 and SnS are 3.70 and 2.31 eV, respectively, and the conduction band minimum (E_{CB}) of Zn_2SnO_4 and SnS are -0.28 and -0.67 eV, respectively. Therefore, according to the equation ($E_g = E_{VB} - E_{CB}$), the valence band maximum (E_{VB}) of Zn_2SnO_4 and SnS are calculated to be 3.42 and 1.64 eV, respectively.⁴⁸

3.2.3. PL analysis. Photoluminescence (PL) spectroscopy is an effective method to illustrate the efficiency of photogenerated carrier recombination.⁴² As a rule, the weaker the PL

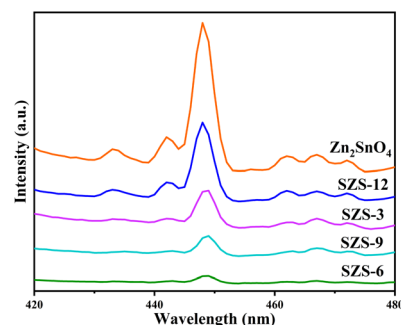


Fig. 5 PL spectra of the Zn_2SnO_4 , SZS-3, SZS-6, SZS-9 and SZS-12.

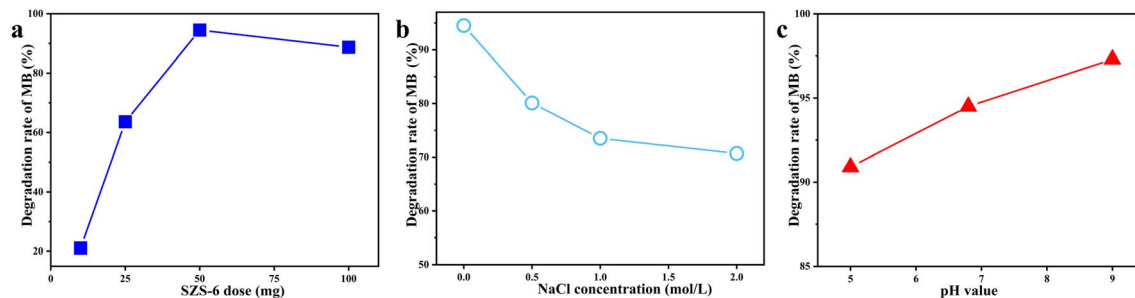


Fig. 6 (a) The effects of operational variables on the photocatalytic response, SZS-6 doses (for degrading 10 mg per L MB), (b) ionic strengths and (c) pH values (for degrading 10 mg L⁻¹ of MB in the presence of 0.05 g of SZS-6).

spectral signal, the lower the ratio of photogenerated carrier recombination.⁴⁹ Fig. 5 indicates the PL spectra of Zn₂SnO₄ as well as SZS-*x*. These samples all show strong PL emission peaks at 449 nm. And Zn₂SnO₄ has the highest PL intensity in these samples, illustrating that the addition of SnS restrains the recombination of photogenerated electron-hole pairs. Meanwhile, the PL intensity of SZS is weakened as the ratio of SnS to Zn₂SnO₄ increases from 3 to 6%. However, the PL intensity of SZS gradually increases when the ratio is further increased to 9 or 12%. The results demonstrate that SZS-6 has the weakest PL intensity, implying that the recombination rate of the photogenerated carriers is the lowest. Based on the above optical properties, the SZS-6 has a higher carrier separation efficiency, improving its photocatalytic activity.

In order to assess the energy efficiency factor in the photocatalytic process under study, the electrical energy per order (EE/O) and the average apparent quantum yield ($\varphi_{\text{app,av}}$) have been calculated (Table S2[†]). Smaller values of the EE/O, less energy is required for decreasing the concentration of model pollutants in the photocatalytic system. The higher the average apparent quantum yield indicates that the more electrons are involved in the photocatalytic system, the more advantageous it is for photocatalytic reactions. The results of EE/O and $\varphi_{\text{app,av}}$ obtained also illustrates that the SZS-6 has the least energy consumption and the most electrons joining the photodegradation.

3.3. Photocatalytic activity tests

3.3.1. Effects of operational variables on the photocatalytic response. Various factors influencing the photodegradation process were studied (Fig. 6). Fig. 6a shows the effect of SZS-6 catalysts dosage on the degradation rate of MB. It can be seen that firstly the active sites of SZS-6 catalysts with increasing the content of SZS-6, inducing rising the degradation rate of MB. However, as the SZS-6 dosage reaches 0.1 g, a decrease in photodegradation of MB is observed, owing to microscopic agglomeration of the photocatalyst. Therefore, the optimal dosage of SZS-6 is 0.05 g, corresponding to 94.5% of the maximum degradation rate of MB.

The effect of ionic strength on the catalytic activity of SZS-6 was studied using different concentrations of NaCl solutions. As shown in Fig. 6b, the increase of ionic strength is not

conductive to the photodegradation of MB. This is because the MB is a negative dye, and Na⁺ can be adsorbed on the surface of MB by electrostatic attraction to reduce the contact MB with SZS-6. In addition, the additional ions also maybe act as charge traps, limiting the quantum yield of the photocatalyst.^{7,51}

The effect of acidity and alkalinity on the activity of SZS-6 was also researched (Fig. 6c). The degradation rate of MB at different pH (5, 6.8, and 9) are 90.9, 94.5, and 97.3%, respectively. The result displays that the alkaline condition is favourable for MB degradation. Considering the high instrumental requirements of alkaline solutions, deionized water is used as the solvent for this experiment.^{52,53}

Meanwhile, the result demonstrates that the temperature has little influence on the photocatalytic performance of SZS-6 under the range of 10–40 °C (Fig. S2[†]).

3.3.2. Photocatalytic activity. The photocatalytic activities of SZS-*x* were investigated by degrading MB under visible light ($\lambda > 420$ nm). As shown in Fig. 7a, the degradation efficiency of pure Zn₂SnO₄ and SnS is only about 41.6% and 41.9% in 1 h irradiation, respectively. As the ratio of SnS to Zn₂SnO₄ increased from 3 to 12%, the photocatalytic activity of SZS-*x* first enhanced significantly and then decreased gradually. And when the ratio of SnS to Zn₂SnO₄ reaches 6%, the degradation efficiency of MB is the highest. Experimental results demonstrate that the SZS-6 can degrade 94.5% of MB over 60 min under visible light. In order to eliminate the effect of dark absorption, the amount of MB adsorbed before light irradiation has been obtained (Table S3[†]). Combined with the result of Fig. 7a and Table S3[†], it can be seen that the degradation MB is mainly photocatalyzed by SZS-6.

The photocatalytic activity of SZS-6 owes to the following reasons: (1) compounding with SnS redshifts the absorption edge of the SZS-6 bandgap, extending the absorption range for visible light; (2) the Z-scheme heterojunction formed in SZS-6 improves the separation efficiency of photogenerated carriers and photocatalytic activity.

Based on Fig. 7b and Table 2, it can be found that all degradation reactions follow the pseudo-first-order rate equation ($\ln(C_0/C_t) = kt$). In which, C_0 and C_t are the concentrations of MB solution dark equilibrium absorption and after irradiation, respectively; k is the slope of the fitted line, namely as reaction rate constant.⁴⁴ Table 2 shows that the rate constants of Zn₂SnO₄, SnS, SZS-3, SZS-6, SZS-9 and SZS-12 are 0.0076, 0.0085,

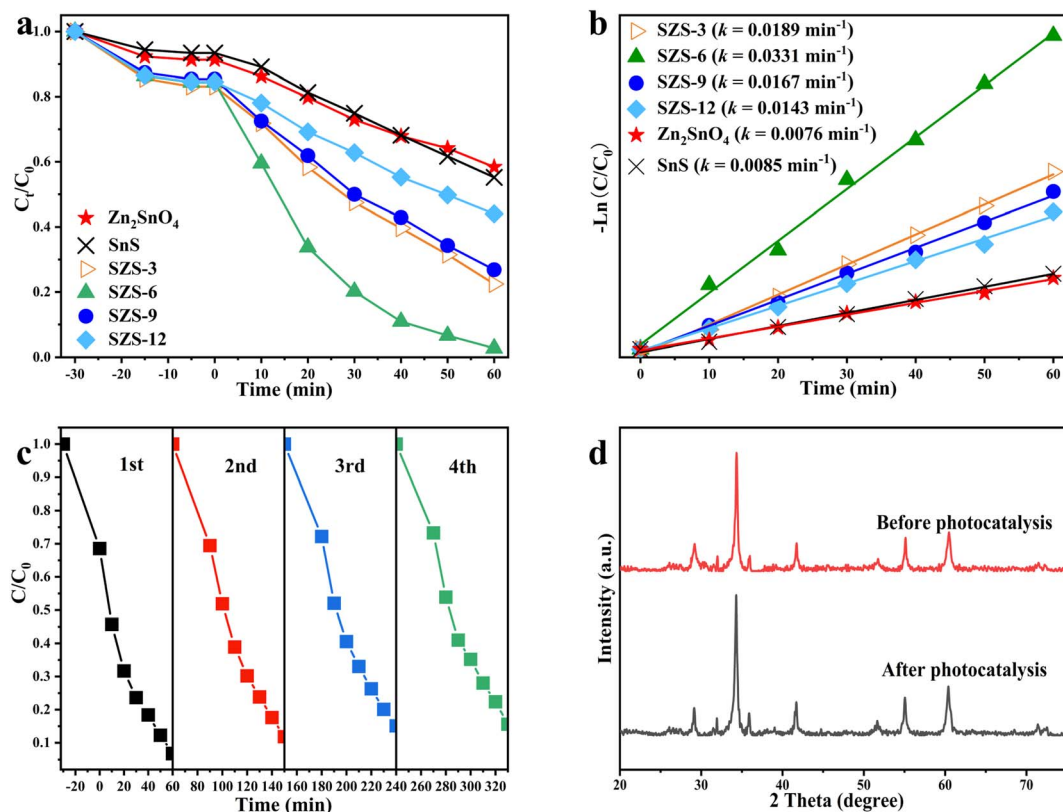


Fig. 7 (a) Photocatalytic degradation and (b) the kinetic curves of MB catalysed by the Zn₂SnO₄, SnS, SZS-x. (c) Cycling tests for the photocatalytic degradation of MB in the presence of SZS-6 and (d) XRD patterns of SZS-6 before and after photocatalysis.

Table 2 Comparison of photocatalytic properties between SnS, Zn₂SnO₄ and SZS-x

Sample	Bandgap (eV)	Degradation rate (%)	<i>k</i> (min ⁻¹)
Zn ₂ SnO ₄	3.7	41.6	0.0076
SnS	2.31	41.9	0.0085
SZS-3	3.66	77.2	0.0189
SZS-6	3.24	94.5	0.0331
SZS-9	3.53	70.6	0.0167
SZS-12	3.57	65.3	0.0143

0.0189, 0.0331, 0.0167 and 0.0143 min⁻¹, respectively. This illustrates that the degradation rate of SZS-6 is the quickest, which is 4.4 times higher than that of Zn₂SnO₄ and it means that the degradation rate of MB increases significantly under the act of the Z-scheme SnS/Zn₂SnO₄ photocatalyst.

In addition, the stability and reusability of the SZS-6 were investigated (Fig. 7c). After the four-cycle tests under visible light, the result displays that the degradation efficiency of MB still holds at 85%. In addition, XRD characterization of SZS-6 was performed before and after the photocatalytic degradation (Fig. 7d). It can be observed that there is almost no

Table 3 Comparing with various photocatalysts for photocatalytic degradation properties reported by references^a

Photocatalyst	Pollutant	The initial concentration of pollutant (mg L ⁻¹)	Volume of pollutant (mL)	Photocatalyst dosage (g)	Degradation time (min)	Degradation (%)	Ref.
Co-doping Na ⁺ CaTiO ₃ :Eu ³⁺	MB	5	100	0.2	300	92.8	33
TiO ₂ /Fe ₂ O ₃	Diazinon	10	100	0.05	45	89.21	54
ZnO/TiO ₂	Diazinon	20	1000	0.5	120	87.26	55
Fe ₂ O ₃ /graphene/CuO	MB	20	100	0.05	40	81.5	56
SrFe ₁₂ O ₁₉	MB	10	50	0.05	270	95	57
Sb ₂ O ₃ /CBO	MB	10	20	0.01	120	90.4	50
Bi ₄ O ₅ Br ₂ /g-C ₃ N ₄	TC	10	100	0.1	60	94	51
SZS-6	MB	10	50	0.05	60	94.5	This work

^a TC stands for tetracyclines.

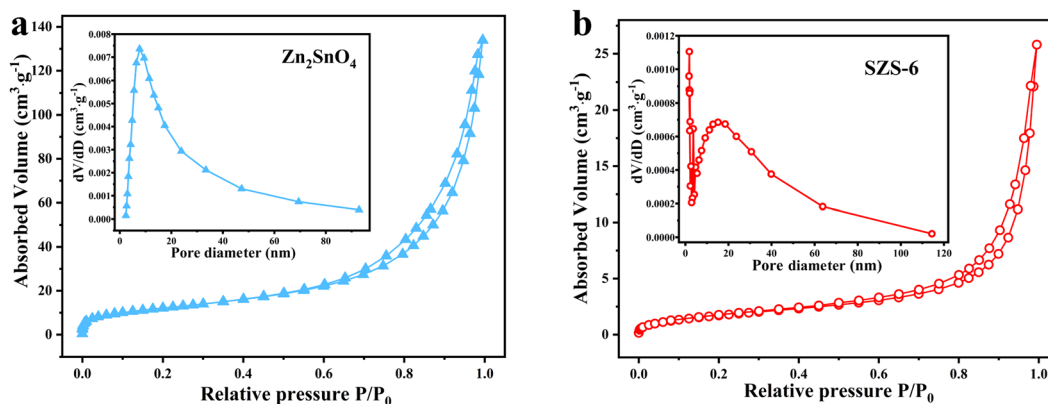


Fig. 8 (a) N_2 adsorption–desorption isotherms of Zn_2SnO_4 and (b) SZS-6, insets are the corresponding pore size distribution.

significantly different in the XRD patterns of SZS-6 before and after the photocatalytic reaction. The result indicates that SZS-6 is stable during photocatalytic degradation.

The degradation performance of the SZS-6 photocatalyst is compared with other references (Table 3). The result indicates that the SZS-6 has improved photocatalytic degradation performance compared to previous studies.

To further verify the degradation performance of SZS-6 to dyes, MO and RhB were used for degradation evaluation by SZS-6 (Fig. S2†). The results show that the degradation rates of RhB and MO are 64.8% and 85.5% in 60 min, respectively. The result illustrates that the SZS-6 catalytic degradation of anionic dyes (MO and MB) is stronger than cationic dye (RhB).

To further confirm that dye adsorption is not the dominant factor in promoting MB degradation, the N_2 adsorption experiment has proceeded. As shown in Fig. 8, both the Zn_2SnO_4 and SZS-6 exhibit reversible type IV hysteresis isotherms with H3 hysteresis loops, illustrating their mesoporous structure. The calculated BET-specific surface area of SZS-6 is $4.44 \text{ m}^2 \text{ g}^{-1}$, which is significantly lower than that of Zn_2SnO_4 ($44.4 \text{ m}^2 \text{ g}^{-1}$) (Table S1†). The insets in Fig. 8 present the Barrett–Joyner–Halenda (BJH) pore size distribution of the Zn_2SnO_4 and SZS-6. From Fig. 8a, it can be observed that the average pore diameter of Zn_2SnO_4 is about 7 nm, while that of SZS-6 is centered at 17 nm (Fig. 8b). Notably, the surface area of SZS-*x* decreased compared to Zn_2SnO_4 , probably due to the stacking of Zn_2SnO_4 in SZS-*x* via SnS. The BET result shows that the SnS

nanoparticles were successfully and uniformly compounded on Zn_2SnO_4 .

To determine the effect of redox potential, cyclic voltammetry was used to test the redox potential of the samples (Fig. S4†). The result shows that the redox potential of samples gradually increases with increasing the content of SnS, indicating that SnS enhanced the redox activity of SZS-*x*.

3.3.3. Photocatalytic mechanism. Generally, a capture experiment is performed to investigate the mechanism of photocatalytic degradation by photocatalysts.^{58,59} For this purpose, different scavengers such as IPA ($\cdot\text{OH}$ scavenger), EDTA-2Na (h^+ scavenger) and BQ ($\cdot\text{O}_2^-$ scavenger) were introduced to evaluate the contribution of different active species to the photodegradation efficiency (Fig. 9a). When adding EDTA-2Na, the photocatalytic degradation rate of MB decreases to 20.6%. And the photocatalytic degradation rate drops to 57.2% or 74.6% for BQ or IPA existence. The above results demonstrate that h^+ plays a major role in the degradation process of MB by SZS-6, while $\cdot\text{OH}$ and $\cdot\text{O}_2^-$ play a minor role during the photocatalytic degradation. Nevertheless, the production of $\cdot\text{OH}$ also needs to consume h^+ , leading to the amount of $\cdot\text{OH}$ produced being meagre; herein, its role can be ignored.

Based on the characteristics of charge transfer from high Fermi energy to low Fermi energy during the formation of heterojunction (charges rearrangement process), the work function of SnS and Zn_2SnO_4 can be calculated using density functional theory (DFT) in Fig. 9b and c.^{21,60}

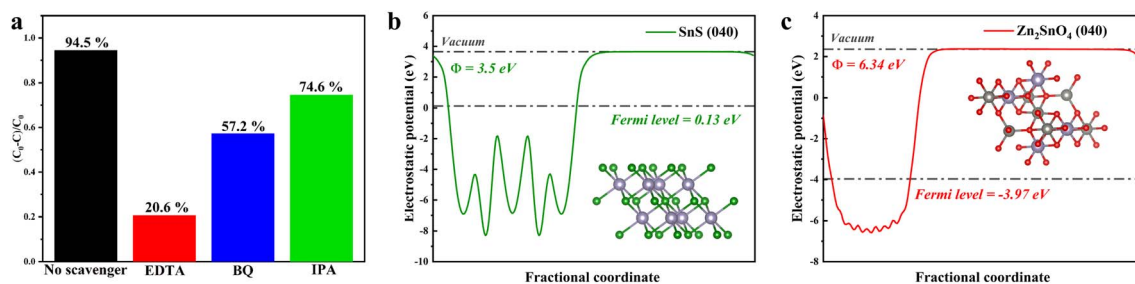


Fig. 9 (a) Effect of different scavengers on the photocatalytic degradation of MB by SZS-6, electrostatic potentials diagrams of (b) SnS and (c) Zn_2SnO_4 .

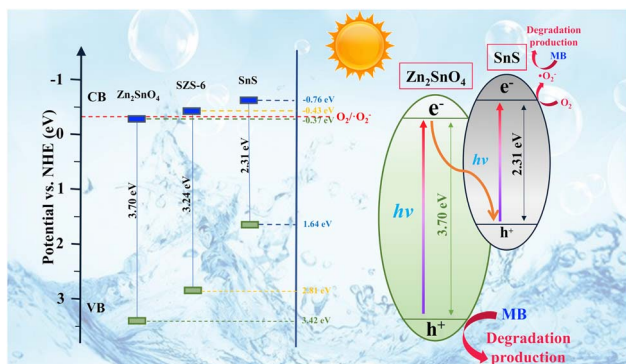
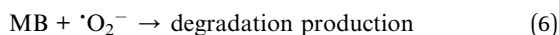
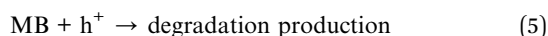
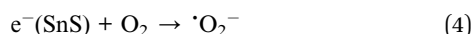
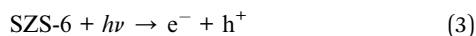


Fig. 10 The degradation mechanism of MB by SZS-*x* under visible-light irradiation.

The work functions of SnS and Zn_2SnO_4 are 3.50 eV and 6.34 eV, respectively. Based on Fig. 4 and 9, it is clear that SnS possesses higher CB and VB positions and a smaller work function than Zn_2SnO_4 . After SnS and Zn_2SnO_4 are intimately contacted, the photogenerated e^- in SnS migrate to Zn_2SnO_4 . Therefore, the interfaces on SnS and Zn_2SnO_4 are positively and negatively charged, respectively, which leads to the formation of built-in electric fields.²⁰ This built-in electric field can accelerate the transfer of the photogenerated e^- and h^+ and promotes the charge transfer from SnS to Zn_2SnO_4 . In the meantime, the built-in electric field and extra potential barrier can significantly restrain other charge migration routes.³⁶ Therefore, it can be determined that a Z-scheme pathway is formed in this system.

Based on the above analysis, a direct Z-scheme charge transfer mechanism is put forward (Fig. 10). Under visible light, Zn_2SnO_4 and SnS are excited synchronously and generate electron-hole pairs. Electrons (e^-) at VB rapidly migrate to CB in the same semiconductor, while a corresponding number of holes (h^+) appear in VB. The e^- in the CB of Zn_2SnO_4 directly transfers to the VB of SnS and recombines with h^+ of SnS.⁶⁴ This induces that the VB of Zn_2SnO_4 has free h^+ and the CB of SnS has free e^- , thus making more active carriers participate in the photocatalytic process (eqn (3)). The h^+ on the surface of Zn_2SnO_4 in SZS-6 oxidates organic dye into colourless intermediates (like aldehyde and acid), and then it is degraded by further oxidation (eqn (5)).^{62,63} In addition, the thermodynamic driving force of e^- in the CB of SnS converts the adsorbed O_2 into $\cdot\text{O}_2^-$ ($E_0(\text{O}_2/\cdot\text{O}_2^-) = -0.33$ eV vs. NHE) (eqn (4)), and the MB dye reacts with $\cdot\text{O}_2^-$, and is degraded (eqn (6)). The reaction mechanism of the photocatalytic degradation for MB dye is as follows.⁶⁴



In a word, the Z-scheme heterojunction formed between Zn_2SnO_4 and SnS effectively promotes the separation efficiency

of the photogenerated carriers to enhance the photocatalytic activity. For MB dye degradation, h^+ is the main active site, while the $\cdot\text{O}_2^-$ group plays a supporting role.

4. Conclusion

In summary, a highly active Z-scheme SnS/ Zn_2SnO_4 photocatalyst had been synthesized successfully. TEM analysis indicated that SnS nanoparticles were well dispersed on the surface of Zn_2SnO_4 polyhedra. HRTEM, XPS and UV-vis DRS proved that a Z-scheme heterojunction was successfully constructed between Zn_2SnO_4 and SnS. As expected, the SnS/ Zn_2SnO_4 showed a much higher photocatalytic activity towards the degradation of MB under visible light. The best photo-degradation rate constant of MB degradation for SZS-6 was as high as 0.0331 min^{-1} , 3.9 and 4.4 times higher than that of SnS and Zn_2SnO_4 , respectively. This enhancement mainly contributed to the formulation of Z-scheme heterojunction between Zn_2SnO_4 and SnS. The Z-scheme heterojunction was helpful for rapid transfer and separation of charge, enhancing its photocatalytic activity. In addition, h^+ is the main active site of MB photo-degradation on SnS/ Zn_2SnO_4 photocatalyst, and the O_2^- group plays a synergistic role. This work provides a novel insight into the sensible design and fabrication of effective Zn_2SnO_4 -based Z-scheme heterojunction photocatalysts for applications in the remediation of the environment and energy conversion.

Author contributions

Yingjing Wang: investigation, writing – original draft, data collecting, experiment design. Fen Xu: writing – review & editing, resources. Lixian Sun: group leader and funding acquisition. Yaying Li: supervision, methodology. Lumin Liao: figure analysis. Yanxun Guan: data collecting. Jianhao Lao: investigation. Yukai Yang: writing review. Tianhao Zhou: data collecting. Yu Wang: formal analysis. Bin Li: data collecting, Kexiang Zhang: TEM image collecting, Yongjin Zou: supervision.

Conflicts of interest

There are no conflicts to declare.

Acknowledgements

This work was supported by the National Natural Science Foundation of China (51971068, U20A20237, 51871065 and 52271205), the Scientific Research and Technology Development Program of Guangxi (AA19182014, AD17195073, AA17202030-1, AB21220027, 2021AB17045), Science Research and Technology Development Project of Guilin (20210216-1, 20210102-4), Guangxi Bagui Scholar Foundation, Lijiang River Scholar Foundation, Guangxi Collaborative Innovation Centre of Structure and Property for New Energy and Materials, Chinesisch-Deutsche Kooperationsgruppe (GZ1528), Guangxi key research and development program (2021AB17045), Science Research and Technology Development Project of Guilin

(20210216-1) and Innovation Project of GUET Graduate Education (2022YCX201).

References

- 1 A. Fujishima, X. Zhang and D. Tryk, *Surf. Sci. Rep.*, 2008, **63**, 515–582.
- 2 G. F. Liao, X. Y. Tao and B. Z. Fang, *Matter*, 2022, **5**, 377–379.
- 3 L. Sun, S. Li, Y. Su, D. He and Z. Zhang, *Appl. Surf. Sci.*, 2019, **463**, 474–480.
- 4 N. Z. Bao, L. M. Shen, T. Takata and K. Domen, *Chem. Mater.*, 2008, **20**, 110–117.
- 5 L. S. Zhang, W. Z. Wang, Z. G. Chen, L. Zhou, H. L. Xu and W. Zhu, *J. Mater. Chem.*, 2007, **17**, 2526–2532.
- 6 Y. Y. Li, F. Xu, L. X. Sun, X. G. Xue, Y. J. Wang, L. M. Liao, Y. X. Guan, B. Li, K. X. Zhang, Y. J. Zou and H. Z. Zhang, *New J. Chem.*, 2022, **46**, 8794–8804.
- 7 F. T. Yi, J. Liu, G. P. Liang, X. Xiao and H. F. Wang, *J. Alloys Compd.*, 2022, **905**, 164064.
- 8 H. Sun and S. J. Park, *J. Environ. Sci.*, 2022, **118**, 57–66.
- 9 G. F. Liao, C. X. Li and B. Z. Fang, *Matter*, 2022, **5**, 1635–1637.
- 10 M. Q. Li, H. Huang, J. X. Low, C. Gao, R. Long and Y. J. Xiong, *Small Methods*, 2018, **3**, 1800388.
- 11 C. K. Govindappa, V. T. Venkatarangaiah and S. B. A. Hamid, *Nano-Micro Lett.*, 2013, **5**, 101–110.
- 12 S. Y. Lee and S. J. Park, *J. Ind. Eng. Chem.*, 2013, **19**, 1761–1769.
- 13 F. T. Yi, J. Q. Ma, C. W. Lin, H. N. Zhang, Y. X. Qian, H. X. Jin and K. F. Zhang, *Chem. Eng. J.*, 2022, **427**, 132028.
- 14 L. Du, H. P. Zhang, M. M. Zhu and M. Z. Zhang, *Inorg. Chem. Front.*, 2019, **6**, 2311–2317.
- 15 L. Q. Sun, X. Han, Z. Jiang, T. T. Ye, R. Li, X. S. Zhao and X. G. Han, *Nanoscale*, 2016, **8**, 12858–12862.
- 16 X. L. Bai, N. Pan, X. P. Wang and H. Q. Wang, *Chin. J. Chem. Phys.*, 2008, **21**, 81–86.
- 17 Q. Q. Zhao, D. X. Ju, X. F. Song, X. L. Deng, M. Ding, X. J. Xu and H. B. Zeng, *Sens. Actuators, B*, 2016, **229**, 627–634.
- 18 T. Yan, H. Y. Liu, M. Sun, X. D. Wang, M. M. Li, Q. Yan, W. G. Xu and B. Du, *RSC Adv.*, 2015, **5**, 10688–10696.
- 19 G. F. Liao, C. X. Li, X. Z. Li and B. Z. Fang, *Cell Rep. Phys. Sci.*, 2021, **2**, 100355.
- 20 G. F. Liao, C. X. Li, S. Y. Liu, B. Z. Fang and H. M. Yang, *Phys. Rep.*, 2022, **983**, 1–41.
- 21 S. Xia, G. Zhang, Z. Gao, Y. Meng, B. Xie, H. Lu and Z. Ni, *J. Colloid Interface Sci.*, 2021, **604**, 798–809.
- 22 P. Zhou, J. Yu and M. Jaroniec, *Adv. Mater.*, 2014, **26**, 4920–4935.
- 23 C. Kim, K. M. Cho, A. Al-Saggaf, I. Gereige and H.-T. Jung, *ACS Catal.*, 2018, **8**, 4170–4177.
- 24 L. Q. Ye, J. Y. Liu, C. Q. Gong, L. H. Tian, T. Y. Peng and L. Zan, *ACS Catal.*, 2012, **2**, 1677–1683.
- 25 K. Maeda, *ACS Catal.*, 2013, **3**, 1486–1503.
- 26 H. W. Guo, S. P. Wan, Y. N. Wang, W. H. Ma, Q. Zhong and J. Ding, *Chem. Eng. J.*, 2021, **412**, 128646.
- 27 D. L. Huang, S. Chen, G. M. Zeng, X. M. Gong, C. Y. Zhou, M. Cheng, W. J. Xue, X. L. Yan and J. Li, *Coord. Chem. Rev.*, 2019, **385**, 44–80.
- 28 S. Jayswal and R. S. Moirangthem, *New J. Chem.*, 2018, **42**, 13689–13701.
- 29 Z. Li, X. Meng and Z. Zhang, *J. Colloid Interface Sci.*, 2019, **537**, 345–357.
- 30 Y. Jiang, Z. Yang, P. Zhang, H. Jin and Y. Ding, *RSC Adv.*, 2018, **8**, 13408–13416.
- 31 L. Li, L. Zheng and G. Shen, *Adv. Funct. Mater.*, 2018, **28**, 1705389.
- 32 D. Zhang, X. Zong, Z. Wu and Y. Zhang, *ACS Appl. Mater. Interfaces*, 2018, **10**, 32631–32639.
- 33 M. Chen, Q. Xiong, Z. Liu, K. H. Qiu and X. Xiao, *Ceram. Int.*, 2020, **46**, 12111–12119.
- 34 S. M. Peymani-Motlagh, A. Sobhani-Nasab, M. Rostami, H. Sobati, M. Eghbali-Arani, M. Fasihi-Ramandi, M. R. Ganjali and M. Rahimi-Nasrabadi, *J. Mater. Sci.: Mater. Electron.*, 2019, **30**, 6902–6909.
- 35 L. Wang, H. Zhai, G. Jin, X. Li, C. Dong, H. Zhang, B. Yang, H. Xie and H. Sun, *Phys. Chem. Chem. Phys.*, 2017, **19**, 16576–16585.
- 36 M. L. Gu, Y. H. Li, M. Zhang, X. M. Zhang, Y. Shen, Y. Q. Liu and F. Dong, *Nano Energy*, 2021, **80**, 105415.
- 37 K. Wang, D. Liu, P. Deng, L. Liu, S. Lu, Z. Sun, Y. Ma, Y. Wang, M. Li and B. Y. Xia, *Nano Energy*, 2019, **64**, 103954.
- 38 T. Ling, D. Y. Yan, Y. Jiao, H. Wang, Y. Zheng, X. Zheng, J. Mao, X. W. Du, Z. Hu, M. Jaroniec and S. Z. Qiao, *Nat. Commun.*, 2016, **7**, 12876.
- 39 C. Y. Wu, C. J. Lee, Y. H. Yu, H. W. Tsao, Y. H. Su, C. C. Kaun, J. S. Chen and J. J. Wu, *ACS Appl. Mater. Interfaces*, 2021, **13**, 4984–4992.
- 40 M. Fakhrazad, A. H. Navidpour, M. Tahari and S. Abbasi, *Mater. Res. Express*, 2019, **6**, 095037.
- 41 E. Keles, M. Yildirim, T. Öztürk and O. A. Yildirim, *Mater. Sci. Semicond. Process.*, 2020, **110**, 104959.
- 42 Y. X. Wang, Y. Q. Yang, L. M. Xi, X. D. Zhang, M. H. Jia, H. M. Xu and H. G. Wu, *Mater. Lett.*, 2016, **180**, 55–58.
- 43 Y. M. Liu, Y. F. Cao, H. Lv, S. Li and H. Zhang, *Mater. Lett.*, 2017, **188**, 99–102.
- 44 J. Liu, J. Ke, Y. Li, B. J. Liu, L. D. Wang, H. N. Xiao and S. B. Wang, *Appl. Catal., B*, 2018, **236**, 396–403.
- 45 R. Tang, S. Zhou, L. Zhang and L. Yin, *Adv. Funct. Mater.*, 2018, **28**, 1706154.
- 46 B. Chen, W. Fan, B. Mao, H. Shen and W. Shi, *Dalton Trans.*, 2017, **46**, 16050–16057.
- 47 Z. Sun, W. Fang, L. Zhao and H. Wang, *Appl. Surf. Sci.*, 2020, **504**, 144347.
- 48 X. J. Zou, Y. Y. Dong, C. Y. Yuan, H. Ge, J. Ke and Y. B. Cui, *J. Taiwan Inst. Chem. Eng.*, 2019, **96**, 390–399.
- 49 R. Wu, H. Song, N. Luo and G. Ji, *J. Colloid Interface Sci.*, 2018, **524**, 350–359.
- 50 M. Azimifar, M. Ghorbani and M. Peyravi, *J. Mol. Struct.*, 2022, **1270**, 133957.
- 51 F. T. Yi, J. Q. Ma, C. W. Lin, L. Y. Wang, H. N. Zhang, Y. X. Qian and K. F. Zhang, *J. Alloys Compd.*, 2020, **821**, 153557.
- 52 M. Moztahida and D. S. Lee, *J. Hazard. Mater.*, 2020, **400**, 123314.

- 53 P. A. Ajibade, T. B. Mbuyazi and A. E. Oluwalana, *J. Inorg. Organomet. Polym. Mater.*, 2021, **31**, 2197–2208.
- 54 S. R. Mirmasoomi, M. Mehdipour Ghazi and M. Galedari, *Sep. Purif. Technol.*, 2017, **175**, 418–427.
- 55 A. Jonidi-Jafari, M. Shirzad-Siboni, J.-K. Yang, M. Naimi-Joubani and M. Farrokhi, *J. Taiwan Inst. Chem. Eng.*, 2015, **50**, 100–107.
- 56 P. Nuengmatcha, P. Porrawatkul, S. Chanthai, P. Sricharoen and N. Limchoowong, *J. Environ. Chem. Eng.*, 2019, **7**, 103438.
- 57 D. D. Mishra and G. Tan, *J. Phys. Chem. Solids*, 2018, **123**, 157–161.
- 58 K. B. Bhojanaa, A. Soundarya Mary, K. S. Shalini Devi, N. Pavithra and A. Pandikumar, *Sol. RRL*, 2021, **6**, 2100792.
- 59 D. Ursu, R. Banică, M. Vajda, C. B. Baneasa and M. Miclau, *J. Alloys Compd.*, 2022, **902**, 163890.
- 60 G. H. Zhang, Y. Meng, B. Xie, Z. M. Ni, H. F. Lu and S. J. Xia, *Appl. Catal., B*, 2021, **296**, 120379.
- 61 K. Gelderman, L. Lee and S. Donne, *J. Chem. Educ.*, 2007, **84**, 685–688.
- 62 A. Takai and P. V. Kamat, *ACS Nano*, 2011, **5**, 7369–7376.
- 63 T. K. Jia, F. Fu, J. Li, Z. Deng, F. Long, D. S. Yu, Q. Cui and W. M. Wang, *Appl. Surf. Sci.*, 2020, **499**, 143941.
- 64 A. Zhu, Q. Zhao, X. Li and Y. Shi, *ACS Appl. Mater. Interfaces*, 2014, **6**, 671–679.